Research article

Evaluating Pb-based and Pb-free Halide Perovskites for Solar-Cell Applications: A Simulation Study

Sonali Mehra [a,b], Mamta [a,b], Jai Tawale [a], Govind Gupta [a,b], V.N. Singh [a,b,*], A.K. Srivastava [a,c], Shailesh Narain Sharma [a,b,**]

[a] *CSIR – National Physical Laboratory, Dr. KS Krishnan Marg, New Delhi, 110012, India*
[b] *Academy of Scientific and Innovative Research (AcSIR), Ghaziabad, 201002, India*
[c] *CSIR – Advanced Materials and Processes Research Institute, Bhopal, Madhya Pradesh, India*

ARTICLE INFO

ABSTRACT

Metal halide Pb-based and Pb-free perovskite crystal structures are an essential class of optoelectronic materials due to their significant optoelectronic properties, optical absorption and tuneable emission spectrum properties. However, the most efficient optoelectronic devices were based on the Pb as a monovalent cation, but its toxicity is a significant hurdle for commercial device applications. Thus, replacing the toxic Pb with Pb-free alternatives (such as tin (Sn)) for diverse photovoltaic and optoelectronic applications is essential. Moreover, replacing the volatile methylammonium (MA) with cesium (Cs) leads to the development of an efficient perovskite absorber layer with improved optical & thermal stability and stabilized photoconversion efficiency. This paper discusses the correlation between the experimental and theoretical work for the Pb-based and Pb-free perovskites synthesised using the hot-injection method at different temperatures. Here, simulation is also carried out using the help of SCAPS-1D software to study the effect of various parameters of $CsSnI_3$ and $CsPbI_3$ layers on solar cell performance. This experimental and theoretical comparative study of the Hot-injection method synthesised $CsPbI_3$ and $CsSnI_3$ perovskites is rarely investigated for optoelectronic applications.

1. Introduction

Metal-halide perovskite crystal structures are potential optoelectronic [1] materials with enhanced optical absorption and emission properties [2,3]. To date, these solution-processed lead (Pb) & lead-free metal halide 3D perovskite [4] were reported for methylammonium, formamidinium, methylhydrazinium [5,6], aziridinium [7,8], and Cs as A-cation in the ABX_3 perovskite lattice. All these Pb & Pb-free perovskite [9] semiconductors [10] have shown great perspective in optoelectronic devices such as solar cells [11], light-emitting diodes [12,13] (LEDs), and lasers [14]. However, the Pb-halide perovskites still face two unresolved issues: Pb-toxicity and its poor stability against heat or moisture, which hinders commercial applications. The stability of Pb-halide perovskites can be improved by replacing the organic cation on the A-site (MA or FA) with an inorganic cation, Cs^+ or Rb^+. It results in inorganic halide perovskite while B cation (Pb) will be replaced by non-toxic Sn^{2+} ion of similar valence configuration & ionic radius to fabricate Pb-free halide perovskites [15]. However, due to the oxidation of tin from Sn^{2+} to Sn^{4+}, Sn-based halide perovskites degrade rapidly

---

under ambient air, leading to lower device performance and high defect density [16] compared to Pb-based analogues [17]. Due to this, all-inorganic Cs-based perovskites exhibit enhanced stability and less defect density compared with MA-based perovskite nanocrystals [18,19]. Hence, Pb-free halide perovskites with strong PL and narrow FWHM are essential for high-resolution & vibrant display-based enhanced optoelectronic applications. Generally, integrating different halides into crystal structure [20] or reducing crystallite size to nanometre scale [21] helps in the band-gap tunability of metal-halide perovskites. Its effect relies on different ionisation potentials of various halide components [22]. Secondly, it reveals the quantum-confined nanostructures where the band gap increases with the reduction in the size of perovskite nanocrystals [23]. Moreover, the quantum confinement of holes and electrons in these nanostructures stimulates effective radiative recombination [24]. It shows high photoluminescence quantum efficiency (PLQE) compared to the bulk perovskite material required for optoelectronic applications [25].

If Pb^{2+} is replaced with Sn^{2+}, these Sn-based perovskites can maintain the 3D perovskite structure well and have significant applications in optoelectronic devices. Due to the higher sensitivity of Sn^{2+}, the literature reports the maximum PLQY of $CsSnX_3$ to less than 1 %. At the same time, vacancy-ordered double perovskite Cs_2SnX_6 with Sn^{4+} possesses good stability but still suffers from poor PLQY. Lead-halide perovskite quantum dots (QDs) & bulk are supple and sensitive to humidity, moisture, light, air, temperature, etc. They pollute the earth due to their toxicity, long degradation time and easy degradation of water solubility. Thus, it creates the need to develop environment-friendly Pb-free perovskite materials for optoelectronic applications [26]. The Sn-based perovskites have achieved 6.4 % of maximum PLQY, which is inferior to Pb-based perovskites with ~84 % PLQY. Besides Sn^{2+}, the replacement of Pb^{2+} with Zn^{2+}, Ge^{2+}, Mn^{2+}, Cu^{2+} & Bi^{2+} metal ions for Pb-free perovskites have been investigated for versatile applications. However, the PL decay in Sn-based perovskite nanocrystals appears on a pico-to-nanosecond time scale through two different radiative decay mechanisms assigned to band-to-band emission and radiative recombination at shallow intrinsic defect sites [27,28]. The optoelectronic properties of perovskites are readily altered by varying the A, B or X site in the ABX_3 perovskite structure [29]. These inorganic Cs Pb & Sn-based iodide perovskite nanocrystals (NCs) have been regarded as a class of materials for their utilization in solar cells, light-emitting diodes, lasers, photodetector applications [30,31]. However, due to their facile synthesis, high photoluminescence quantum yield (PLQY), and high color purity, $CsPbX_3$-based LEDs exhibit efficient and high-speed emission under high-frequency modulation, making them good candidates for lighting sources in visible light communication (VLC).

Perovskite nanocrystals (NCs) are used instead of films for solar cell devices due to their unique properties. Perovskite NCs exhibit high carrier mobility, reduced trap density, and improved charge transport properties compared to perovskite films [32]. Moreover, the perovskite NCs show band-gap tunability due to the quantum confinement effect, while thin films do not show any quantum confinement effect. Thus, the perovskite NCs' unique characteristics help enhance solar cell devices' light absorption efficiency and stability.

Generally, band-gap energy levels of hybrid perovskites are determined by an anti-bonding hybrid state between cation B-s and anion X-p orbitals [33]. However, the band-gap tuning mechanism is due to the hybridisation of p- and s-orbitals, as the Br-4p orbital overlaps with the I-5p orbital and the Pb-6s orbital. Similarly, band-gap can be tuned by varying the halide ion concentration in halide perovskites [34,35]. Whereas, tuning of band-gap also includes the substitution of organic A cation by inorganic cation or mixing of both organic and inorganic cations because, with a change in A cation, bond length with B & X site is also changed, leading to band-gap tuning [36]. It is because the electronegativity difference between Sn & I is higher than the electronegativity difference between Pb & I. It implies that the higher electronegativity difference between Sn & I increases the force of attraction with the decrease in bond length, leading to a higher band gap for $CsSnI_3$. However, due to the less electronegativity difference between Pb & I, bond length increases with a lower band gap in $CsPbI_3$ than in Sn-halide perovskites. It complies with the above statement that the change in the bond length of B & X leads to the tuning of the band-gap [37]. Therefore, it is observed that Cs-based all-inorganic ($CsPbI_3$ & $CsSnI_3$) perovskite quantum dots show better performance, high PL quantum yield, narrow emission bandwidth, significant extinction coefficient, crystal defect tolerance, and good stability against moisture and oxygen as compared to organic-inorganic hybrid perovskite quantum dots [38]. These materials are gaining popularity for producing perovskite-based solar cells because of their excellent optoelectronic properties. Device optimization [39] is essential to have an optoelectronic device with the appropriate functionality.

This paper discusses the rare investigation for the experimental and theoretical comparative study of the Hot-injection method synthesised $CsPbI_3$ and $CsSnI_3$ perovskites synthesised at different temperatures. Here, the structural, optical and morphological properties of Pb-based and Pb-free halide perovskites were studied using XRD, UV–Vis, PL, FE-SEM and TEM characterizations with temperature variation. The studies reveal that in contrast with $CsPbI_3$, Sn-based halides exhibit a higher band-gap (3.73 eV) with a decrease in size and higher average lifetime (5.09 ns) at a lower temperature, indicating an efficient replacement of Pb with Sn for Pb-free halides. In this work, we simulate the $CsPbI_3$ and $CsSnI_3$-based solar structures with the help of Solar Cell Capacitance Simulator (SCAPS-1D) software by varying the absorber layer's thickness [40]. Results stated that the $CsSnI_3$ (6.11 %) based solar structure depicts higher efficiency than $CsPbI_3$ (3.76 %). This approach can give an insight into how the thickness of layers impacts the output characteristics of the device.

2. Experimental technique

Materials: All the chemicals required for syntheses such as Tin (II) iodide (SnI_2, 99.99 % trace metals basis), Lead (II) iodide (PbI_2, 99.99 % trace metals basis), Cesium Carbonate (99.99 %, metals basis), Oleyl-amine (OLA, 70 %), Oleic-acid (OA, 90 %), Octadecene (ODE, 90 %), and Tri-octyl phosphine (TOP, 90 %) were purchased from Sigma Aldrich. All the chemicals were used without any further purification.

In a typical synthesis, $CsPbI_3$ and $CsSnI_3$ halide perovskites were synthesised using the hot-injection method at different temperatures, and the diagrammatic representation of this method is shown in Fig. 1. Here, 4 mM of Cs_2CO_3 was added in the stoichiometric

ratio of 1:1 of OLA: OA in 100 ml 3-neck RBF with continuous stirring. The solution was heated to 100 °C under the Argon atmosphere until the clear solution was obtained (for around 1 h). The temperature was increased slowly to 200 °C. On the other hand, 2 mM PbI_2 precursor dissolved in a stoichiometric mixture of ODE & OLA was used as the injection solution for this synthesis. After the required temperature was attained, the PbI_2 solution was injected rapidly into the reaction solution under the argon atmosphere. After injection, the temperature was maintained at 200 °C for a specific time of 10 min. After 10 min, the heat source was removed, and the solution was cooled to 60 °C under normal atmospheric conditions.

Further, the solution obtained was centrifuged at 5500 rpm for 5 min and discarded into the supernatant. Later, it was rewashed with toluene and centrifuged at 8000 rpm for 7 min, and the supernatant thus obtained was utilised for characterisation. A similar procedure was performed by varying the temperature to 250 °C instead of 200 °C to synthesise $CsPbI_3$ at a higher temperature.

Similarly, $CsSnI_3$ were also synthesised using the same hot-injection technique. For $CsSnI_3$ synthesis, SnI_2 dissolved in TOP along with Cs_2CO_3 was used. The synthesis was carried out at 200 & 250 °C [41].

Here, the addition of capping ligands is very crucial in the synthesis of halide-based colloidal perovskites. Oleyl-amine helps control the crystallisation process and provides a colloidal solution, and it will also help stabilise the halide perovskites. However, without adding oleic acid to the synthesis, the colloidal solution becomes cloudy after storage for 24 h. Oleic acid also plays an essential role in suppressing the aggregation effects and helps to stabilise the halide perovskite [42]. Moreover, toluene is used for washing the perovskites because its reaction kinetics is slow and leads to the destruction of colloidal particles during centrifugation due to the high sensitivity and instability of halide-based perovskites [25].

Table 1 compares previously fabricated Cs-based Pb & Pb free iodide perovskite devices and their efficiency for solar-cell applications. All the Pb & Sn iodide perovskites discussed in the table were synthesised using either vapor or solution deposition methods. However, chemically synthesised perovskite has also undergone post-treatment to enhance the efficiency of the perovskite films. On the other hand, this article shows the synthesis of Cs Pb & Sn iodide perovskites using the Hot-injection Method and studies their properties via numerical simulation with respect to thickness variation in halide perovskites. We have synthesised $CsPbI_3$ & $CsSnI_3$ at 200 & 250 °C using the Hot-injection method. Simulation studies show that Sn-halide perovskites exhibit higher conversion efficiency than Pb-iodide perovskites. Although Sn-iodide perovskites were less stable as per literature, chemically synthesised Sn-iodide perovskites were comparatively more stable for device applications. At the same time, the author tries to correlate these results with experimental results of device fabrication in future studies. Therefore, we have observed the previously fabricated Cs Pb & Sn iodide perovskite device performance to study the exciting aspects of the chemically synthesised stable Cs– Pb & Sn iodide perovskites.

3. Simulation technique and solar structure

Numerical modelling has gained popularity in recent years due to its ability to explain the design and function of many solar cell parameters. Perovskite layer thickness can play an essential role in the efficiency of the solar device. In the present work, SCAPS simulates the thickness of these perovskite layers ($CsSnI_3$ and $CsPbI_3$). The Poisson equation and continuity equations for electrons and holes (Equations. (1) – (3)), which are used to calculate the solar cell characteristics, are fundamental to the analysis of this software [52].

$$\frac{d^2}{dx^2}\psi(x) = \frac{-q}{\varepsilon_0\varepsilon_r}\, p(x) - n(x) + N_D - N_A + \rho_P - \rho_n \tag{1}$$

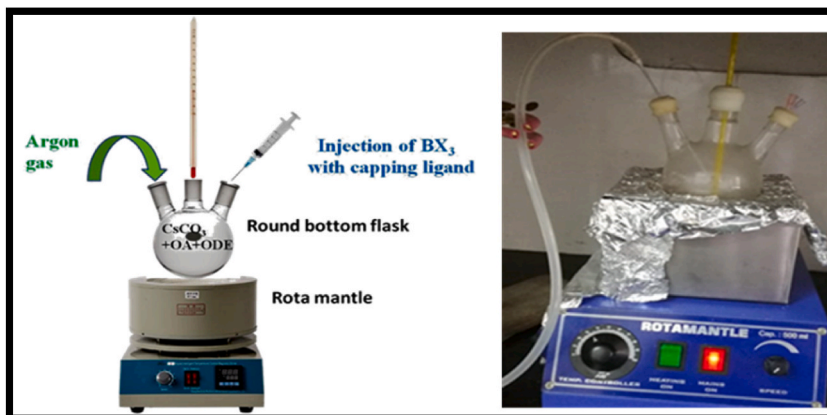$$-\frac{1}{q}\frac{dJ_n}{dx} = (G - R) \tag{2}$$

Fig. 1. Diagrammatic representation of hot-injection technique.

Table 1
Comparison of previously fabricated CsPbI$_3$ & CsSnI$_3$ perovskite devices.

S.No.	Device Architecture	Synthesis Method	V$_{OC}$ (V)	J$_{SC}$ (mA/cm^2)	FF	PCE (%)	Reference
1.	c-TiO$_2$/CsPbI$_3$/P3HT/Au	Vapor-Deposition	1.06	13.8	71.6	10.5	[43]
2.	SnO$_2$/CsPbI$_3$/Spiro/Ag	Vapor Deposition	1.00	13.0	68	8.8	[44]
3.	c-TiO$_2$/CsPbI$_3$–NCs/Spiro/MoO$_x$/Au	Methyl acetate purification	1.23	13.47	65	10.77	[41]
4.	c-TiO$_2$/α-CsPbI$_3$ NCs/PTAA/MoO$_3$/Ag	Spin-coating	1.25	13.83	72	12.3	[45]
5.	PEDOT: PSS/CsPbI$_3$/PCBM/Al	Solution Deposition	0.79	0.26	45	0.09	[46]
6.	m-TiO$_2$/CsPbI$_3$/P3HT/MoO$_3$/Au	Spin-coating	0.35	4.23	0.35	0.52	[47]
7.	c-TiO$_2$/CsPbI$_3$ NCs-CsAc/Spiro/MoO$_x$/Ag	Chemical Synthesis with Post-treatment	1.25	14.96	75.6	14.10	[48]
8.	c-TiO$_2$/CsSnI$_3$/Spiro-MeOTAD/Au	Vacuum Melt Process	0.86	23.2	65	12.96	[49]
9.	ITO/CuI/CsSnI$_3$+10 % SnI$_2$/C$_{60}$/BCP/Al	Vapor Deposition + Solid State Reaction	0.55	8.5	55	2.1	[50]
10.	FTO/TiO$_2$/Cs$_2$SnI$_6$/P3HT/Ag	Spin-coating	0.51	5.41	35	0.96	[51]

$$\frac{1}{q}\frac{dJ_p}{dx} = (G - R) \qquad (3)$$

here ε_r, and ε_0 are relative, and vacuum permittivity. p and n show the number of holes and electrons, N$_A$ and N$_D$ show the acceptor and donor density and R and G show recombination and generation rates, respectively.

Hole transport layer (HTL) based solar cell's device structure is taken Au/CuI/CsSnI$_3$, CsPbI$_3$/CdS/ZnO, where CsSnI$_3$ and CsPbI$_3$ are the absorber layers, CuI is the HTL layer, ZnO is the buffer layer, and Au serves as the back contact metal work function as shown in Fig. 2.

The absorber layers' thickness varied during the simulation, but the parameter values of the buffer and window layers remained unchanged. The SCAPS-1D software's numerical simulation computations are carried out using the various baseline solar cell parameters as inputs. The critical parameters for CsSnI$_3$[53], CsPbI$_3$, ZnO [54], and Cu$_2$O [55] are summarized in Table 2, taken from the literature. Based on the device structure, the energy transfer has been explained using the energy level band diagram in Fig. 3.

Fig. 3 (a & b) shows the energy level band-diagram for CsSnI$_3$ and CsPbI$_3$ perovskites-based devices to understand the carrier dynamics, respectively. Here, E$_c$ denotes the bottom of the conduction band, and E$_v$ denotes the top of the conduction band. Here, the difference between E$_c$ and E$_v$ gives the bandgap (E$_g$) of the material. A slight offset between the valence band & conduction band leads to generating electron-hole pairs within the device. The associated electric field at absorber/HTL and absorber/ETL ensured the movement of light-generated electrons towards ETL and holes towards HTL in perovskite-based devices. Generally, for the basic functioning of solar-cell devices, the band offset of the absorber layer with the transport layer should be as minimal as possible. However, the increase in work function also increases the barrier in the energy band diagram, leading to the degradation of device performance. This is because the high value of the work function creates a barrier for the flow of electrons at the interface of ETL and front contact. On the other hand, the charge carrier dynamics is also affected by the thickness of the perovskite layers. Thus, the thickness should be optimized to thoroughly understand and maintain the carrier dynamics in the energy level band-diagram [56].

4. Characterization

XRD patterns of Cs-based Pb-and Pb-free iodide perovskites were analysed using a Rigaku X-ray Diffractometer. The diffraction pattern was recorded using Cu Kα wavelength (λ = 1.54056 Å) at a step rate of 0.02 min^{-1}. Transmission Electron Microscopy studied
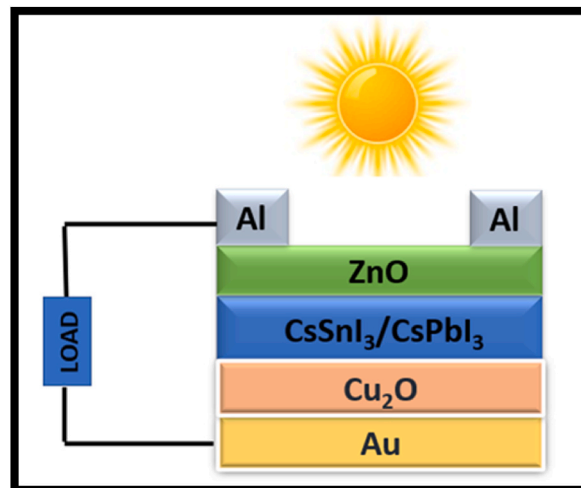
Fig. 2. Schematic of CsSnI$_3$ and CsPbI$_3$-based solar structure.

Table 2
Simulation solar-cell parameters for Perovskite & other layers.

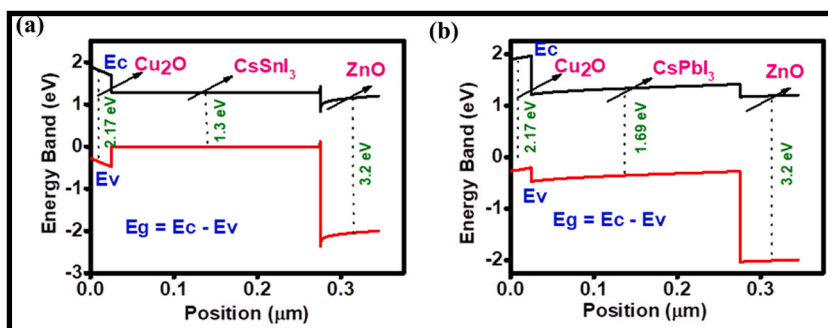| Parameters	$CsSnI_3$	$CsPbI_3$	ZnO	Cu_2O
Thickness (nm)	250	250	70	25
Band Gap (eV)	1.3	1.69	3.2	2.17
Electron Affinity (eV)	3.6	3.95	4.2	3.2
Permittivity	10	6	9	7.1
CB/VB Effective density of states ($1/cm^3$)	$10^{19}/10^{18}$	$10^{20}/10^{20}$	$10^{18}/10^{19}$	$10^{20}/10^{20}$
Electron Mobility(cm^2/Vs)	150	25	200	20
Hole Mobility(cm^2/Vs)	50	25	5	80
Acceptor Density ($1/cm^3$)	1×10^{19}	1×10^{15}	1×10^{15}	1×10^{15}
Donor Density ($1/cm^3$)	0	0	0	1×10^{16}

Fig. 3. Energy level band-diagram for (a) $CsSnI_3$ and (b) $CsPbI_3$ perovskites.

the average particle size of perovskites (TEM), make & model JEOL JEM-1011 (JEOL Ltd. Inc., Tokyo Japan) operated at 80–100 kV. The morphology of $CsPbI_3$ and $CsSnI_3$ perovskites was determined using Field Emission-Scanning Electron Microscopy (FE-SEM), model TESCAN MAGNA GMH. UV absorption spectra of halide perovskites were determined using Ocean Optics 400 tabletops UV–Visible spectrophotometer. PL and TRPL studies of $CsPbI_3$ and $CsSnI_3$ perovskites were determined using an Edinburgh instrument equipped with a xenon lamp, model FLS 980, at different excitation and emission wavelengths for halide variation. The TRPL was studied using the same device, the femtosecond laser. TRPL study helps to determine the average carrier lifetime required by the different halide perovskites. Thus, the supernatant material obtained after the above synthesis in the case of all the perovskites was utilised in a liquid or thin film for various characterizations.
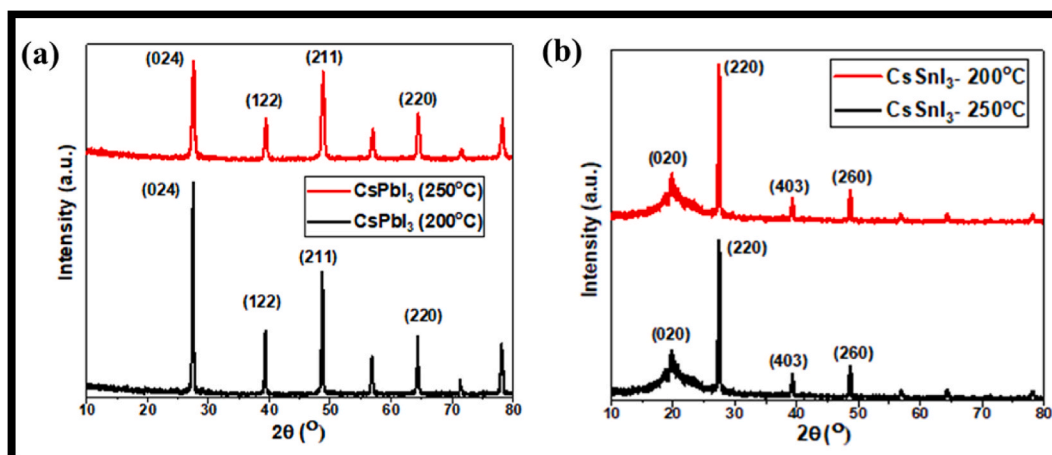

Fig. 4. X-ray Diffraction patterns of (a) $CsPbI_3$, & (b) $CsSnI_3$ perovskite samples at 200 & 250 °C.

5. Results and discussions

5.1. X-ray diffraction study

The precursors Cs_2CO_3, PbI_2, and SnI_2 used in hot-injection synthesis were of high purity and procured commercially from Sigma Aldrich. Fig. 4 (a & b) depicts the XRD pattern of $CsPbI_3$ and $CsSnI_3$ perovskites synthesised at 200 °C & 250 °C, respectively. XRD patterns of the $CsPbI_3$ & $CsSnI_3$ perovskite reveal the improved crystalline structure of the all-inorganic halide perovskites. Here, the XRD spectra of $CsPbI_3$ synthesised at 200 °C show diffraction peaks at 2Θ values 27.5, 39.3, 48.6, and 64.3, corresponding to (024), (122), (211), and (220) lattice planes. In contrast, $CsPbI_3$ perovskite synthesised at a higher temperature of 250 °C shows a slight peak shift from 200 °C synthesised perovskite at similar 2θ values for corresponding lattice planes. Similarly, in the case of $CsSnI_3$ perovskite synthesised at 200 °C, diffraction peaks appeared at 2θ values 19.8, 27.5, 39.2 and 48.7 corresponding to (020), (220), (403) and (260) lattice planes. In contrast, $CsSnI_3$ perovskite synthesised at a higher temperature of 250 °C shows the peak shift towards the lower 2θ value. The broader peaks in the XRD pattern of $CsPbI_3$ reveal a smaller crystallite size, while the narrow peaks in the XRD pattern of $CsSnI_3$ show the larger crystallite size of the Pb-free perovskite samples.

The crystallite size and strain in perovskite samples were evaluated using Williamson-Hall plot [57] for diverse applications of perovskite in solar cells (W–H plot [58] was explained in the supporting information).

Using the W–H plot in Fig. 5, the crystallite size for $CsPbI_3$ was calculated to be 18.12 nm and 22.28 nm at 200 °C and 250 °C, respectively. In contrast, for $CsSnI_3$, the crystallite size was larger than Pb-based halide perovskite and calculated to be 70.45 and 78.37 nm at 200 °C and 250 °C, respectively.

As reported, the increase in crystallite size leads to reduced crystal defects due to lattice strain [59], a lowering trap-state density and an increase in electron lifetime. However, the lattice strain was calculated as 0.0062 and 0.0084, corresponding to $CsPbI_3$ at 200 °C and 250 °C, respectively. In contrast, the lattice strain was computed to be 0.0034 and 0.0073 for $CsSnI_3$ at 200 °C and 250 °C, respectively. The lower strain value in $CsPbI_3$ and $CsSnI_3$ at lower temperatures leads to lower crystal structure distortion, resulting in lesser imperfection in the lattice and crystal defects compared to higher strain value in Pb-based and Pb-free halide perovskites at 250 °C. The crystallite size value obtained from the W–H plot and Debye Scherrer equation are near each other in the literature. Table 3 shows all the structural parameters obtained experimentally for the halide perovskite samples.

Moreover, the Pb-based and Pb-free perovskite crystallise in different phases at room temperature, as $CsPbI_3$ crystallise in cubic phase at 200 & 250 °C, whereas $CsSnI_3$ crystallise in the orthorhombic phase at both the synthesis temperatures. For $CsPbI_3$, all the lattice constants were equal and calculated to be $a = b = c = 7.54$ Å & 7.52 Å at 200 & 250 °C, respectively. These lattice parameter values are very close to the reported value. Here, the unit-cell volume of perovskite samples is calculated using the equation [60] (1):

$$V = a^3 \, (\text{Å})^3 \tag{4}$$

Where a is the lattice parameter of the $CsPbI_3$ perovskite samples. And the X-ray density (ρ) was calculated using the equation [58](2):

$$\rho = \frac{8M}{N_A a^3} \tag{5}$$

where M = molecular weight of perovskite sample.

a = lattice parameter.

N_A = Avogadro constant.

Using the above equations (1) and (2), the volume was calculated to be 428.66 and 425.26 $Å^3$ at 200 & 250 °C, respectively, while the computed density was approximately the same at 22.72 g/cm^3 at both the synthesis temperatures, and these values are in good
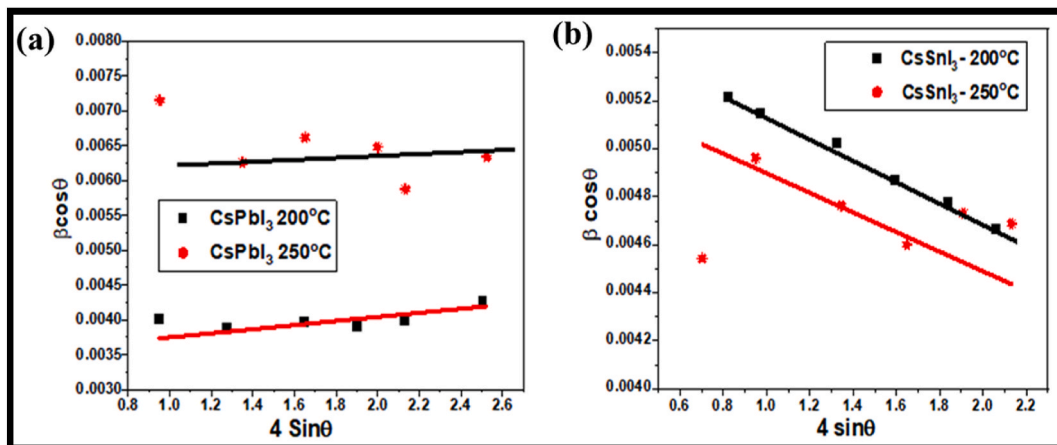

Fig. 5. W–H plots for (a) $CsPbI_3$, and (b) $CsSnI_3$ Perovskite samples at 200 & 250 °C.

Table 3

Structural parameters of CsPbI$_3$ & CsSnI$_3$ halide Perovskites.

| Sample Name	Crystallite size (nm)	Strain	Phase	Lattice Parameters (Å)			Volume (Å) [3]	Density (g/cm^3)
	W–H plot			a	b	c		
CsPbI$_3$ (200°C)	18.12	0.0062	Cubic	7.54	7.54	7.54	428.66	22.72
250°C	22.28	0.0084	Cubic	7.52	7.52	7.52	425.26	22.72
CsSnI$_3$ (200°C)	70.45	0.0034	Ortho-rhombic	9.48	8.98	29.28	2492.62	0.0034
250°C	78.37	0.0073	Ortho-rhombic	9.53	8.94	27.05	2304.61	0.0036

correlation with the reported literature. CsSnI$_3$ crystallises in the orthorhombic phase, and its lattice parameters possess the relation: $a \neq b \neq c$. These parameters were calculated as a = 9.48 Å, b = 8.98 Å and c = 29.28 Å at 200 °C. In contrast, the lattice parameters calculated at 250 °C were slightly varied from that of 200 °C. They determined to be a = 9.53 Å, b = 8.94 Å, c = 27.05 Å. Using the relation between volume and lattice parameters, $\mathbf{V = abc}$, the volume for CsSnI$_3$ was calculated to be 2492.62 (Å) [3] and 2304.61 (Å) [3] at 200 & 250 °C respectively. Although, the density of CsSnI$_3$ perovskite can be computed using the equation [60] (3):

$$\rho = \frac{8M}{abc. \ N_A} \tag{6}$$

and calculated to be 0.0034 and 0.0036 g/cm^3 at 200 & 250 °C, respectively, which agrees with the literature values of Pb-free CsSnI$_3$ halide perovskite samples.

5.2. Optical and photoluminescence spectra

Perovskite materials are known for their unique optoelectronic properties, enhanced photoluminescence (PL) characteristics, long carrier lifetime, and strong absorption, making them a promising candidate for solar cells. Absorbance and Photoluminescence (PL) measurements of perovskite materials help to reveal the optical band gaps from visible to the near-IR region in solution and under an inert atmosphere. However, the band-gaps of Pb-free tin-based perovskite nanocrystals are red-shifted compared with Pb-based perovskites because of the high electronegativity of Sn-ion engaging the 'B' site in the ABX$_3$ perovskite structure [29]. The variation in halide composition can be managed pre- or post-synthesis via different anion-exchange methods using pure-halide perovskites. It
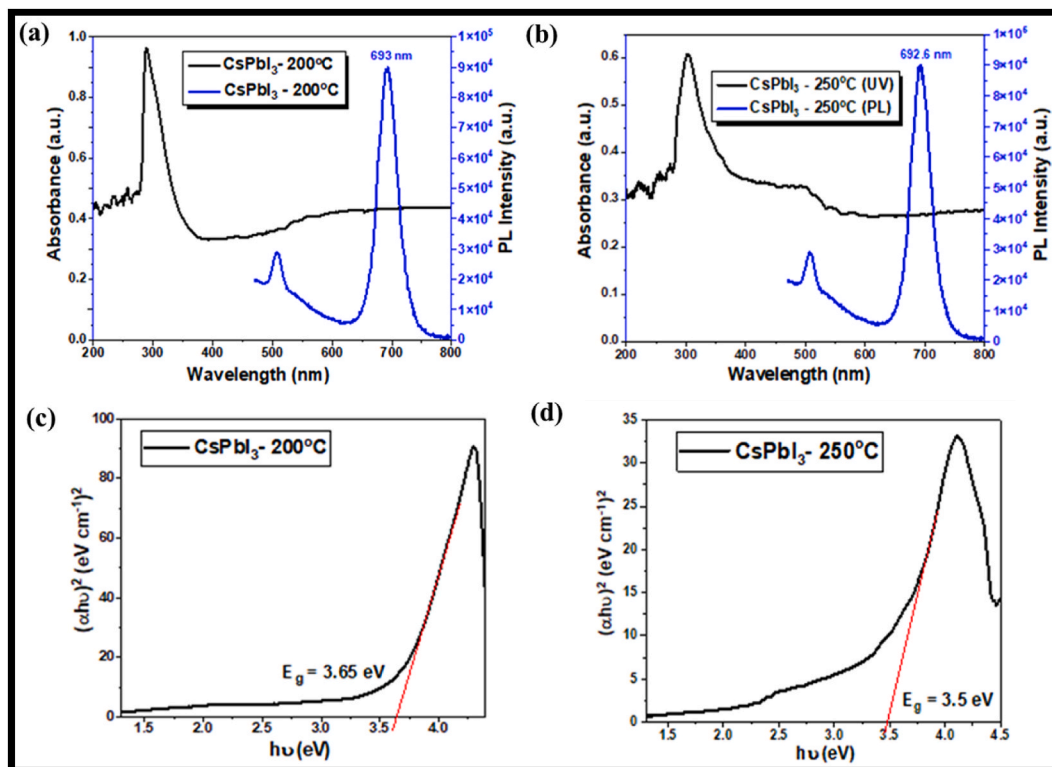
Fig. 6. UV–Vis & PL spectra of CsPbI$_3$ perovskites at (a) 200 °C & (b) 250 °C, and (c) Tauc's Plot for CsPbI$_3$ perovskites at (c) 200 & (d) 250 °C respectively.

would lead to the optical band-gap tuning and affect the optical properties of Pb-based and Pb-free perovskite materials.

Other than tuning the B site, variation in synthesis temperature from 200 °C to 250 °C of CsSnI$_3$ & CsPbI$_3$ nanocrystals allows the tuning in absorption wavelength, leading to the decrease in band-gap from 3.73 eV to 3.63 eV for CsSnI$_3$ and 3.65 eV–3.5 eV for CsPbI$_3$. The wavelength tuning behaviour is constant with the CsPbI$_3$ & CsSnI$_3$ perovskite nanocrystals, revealing the weaker quantum confinement effect of different sized Pb-based & Pb-free perovskites synthesised at different temperatures. In the case of CsSnI$_3$ perovskites, it was observed that a lower synthesis temperature of around 200 °C yields colloidally stable perovskite nanocrystals. In contrast, post-synthesis purification of these nanocrystals forms particle dispersions which show optical properties similar to that of CsSnI$_3$ perovskites synthesised at 200 °C, and this property obstructs determining the exact particle size using TEM for Sn-based perovskites. Fig. 6 (a & b) & Fig. 7 (a & b) shows the UV–Vis & PL spectra of CsPbI$_3$ and CsSnI$_3$ at 200 & 250 °C respectively [61]. Band-gap was calculated using Tauc's plot [62,63], as explained in supporting information.

In the case of indirect band-gap, the photon passed through the intermediate state and did not emit directly. It also transfers the momentum of a crystal lattice. In direct-band-gap transition, the emission of a photon is due to the identical momentum of the hole and electron in the conduction band and valence band [64], respectively.

Further, the graph was plotted between $h\upsilon$ on the *x*-axis and $(\alpha h\upsilon)$ [2] on the *y*-axis, and extrapolating the graph to obtain the band-gap of the halide perovskite samples [65,66] as shown in Fig. 6 (c & d) & 7 (c & d). Moreover, the absorption band-edge shows minimal variation in wavelength as moving towards Pb-free perovskites from Pb-based perovskites in the 400–800 nm wavelength range. These optical properties were also affected in Pb & Sn-based perovskites for the halide composition. Although, the results also inferred that the optical band gap varies in Pb-based and Pb-free halide perovskites. Here, the iodide ion-based Pb & Sn-perovskites show higher band-gap at a lower temperature, and the extrapolation creates large iodine cavities for organic molecules. However, the Sn analogues demonstrate the few characteristics of good electrical conductors and intense room-temperature photoluminescent materials at near-infrared wavelengths [67]. Generally, the band gap and size of the nanoparticles are inversely related. Thus, the band gap increases with the decrease in particle size or vice-versa. Therefore, it can be concluded that higher band-gap or blue-shift in absorption spectra in Pb & Sn-based free halide perovskite samples have promising applications in sensors, solar cells and photodetectors [68].

Photoluminescence measurements were measured using a PL spectrophotometer of 300–800 nm. These Pb-based & Pb-free perovskites show intense PL spectra in the visible region under the excitation range of 350 nm. The Sn analogues demonstrate the few characteristics of good electrical conductors and intense room-temperature photoluminescent materials at near-infrared wavelengths. PL intensity increases with an increase in temperature for Pb & Sn-based perovskites, whereas Pb-based perovskites exhibit higher PL intensity than Sn-based perovskites.
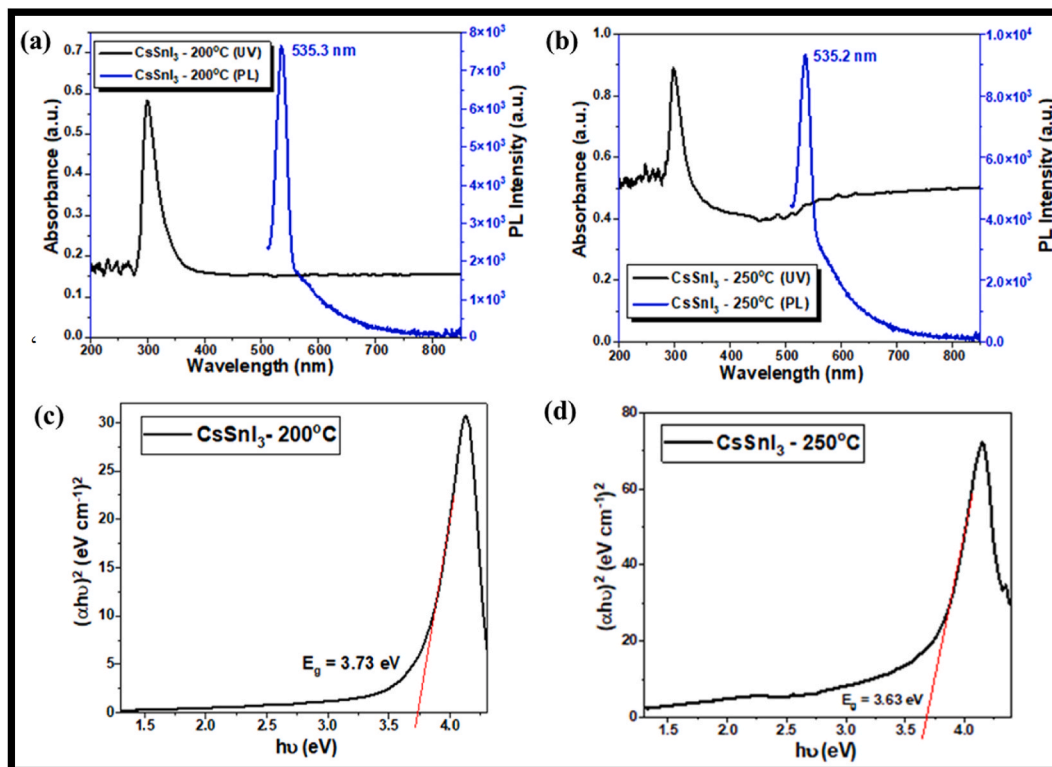

Fig. 7. UV–Vis & PL spectra of CsSnI$_3$ perovskites at (a) 200 °C, & (b) 250 °C, and (c) Tauc's Plot for CsSnI$_3$ perovskites at (c) 200 °C, & (d) 250 °C respectively.

The Cs-based Pb- & Pb-free halide perovskite shows narrow band PL emission at a temperature range of 200 & 250 °C. These Pb-based & Pb-free perovskites show strong and narrow PL emission in the 400–800 nm range. PL spectra of $CsPbI_3$ show narrow PL emission at 692 & 691 nm, corresponding to a temperature range of 200 and 250 °C, respectively. Similarly, the PL spectra of $CsSnI_3$ show narrow PL emission at 536 & 535 nm, corresponding to the temperature of 200 & 250 °C. With temperature variation, redshift PL emission with a narrower peak was observed, leading to low material trap density.

Moreover, the PL emission peak was observed at different excitation wavelengths of 440 nm and 508 nm corresponding to $CsPbI_3$ and $CsSnI_3$, respectively, in the given temperature range. This difference in excitation spectra was attributed to the inorganic part of the perovskite structure [69]. However, PL intensity varies in Pb-based & Pb-free halide perovskites and with temperature variation due to structural distortion in the compounds. Thus, it can be inferred that the significant PL emission peak originated from the Pb inner band, which lies between the Pb (6p) and Pb (6s) bands. These PL peaks suggested an independent behaviour from halide ion orbital mixing [70].

We suggest that the significant PL emission peak originated from the Pb inner band, which lies between the Pb (6p) and Pb (6s) bands, based on their analysis of the electronic band structure of the halide perovskite. In $CsPbI_3$ perovskite, the electronic band structure consists of energy bands formed by the atomic orbitals of the constituent elements.

Here, the Pb atoms in $CsPbI_3$ contribute to forming valence and conduction bands through their electronic orbitals. The valence band is primarily composed of the 6s and 6p orbitals of the lead (Pb) atoms and the 5s and 5p orbitals of the iodine (I) atoms, while the conduction band is composed using the 6p orbitals of the Pb atoms [71,72]. However, within the energy range between the Pb (6p) and Pb (6s) bands, additional electronic states may exist related to the Pb inner band. Thus, it was observed that the significant PL emission peak is attributed to the transitions of electrons between these states within the Pb inner band. When charge carriers (electrons & holes) recombine across this Pb inner band, they emit photons with specific energies corresponding to the material's band gap. Therefore, the theoretical understanding provides insights into the electronic structure of perovskites and explains the results in the PL emission peak originating from the Pb inner band. It is worth noticing that the exact location and nature of electronic states within the material's band gap can be complex and may vary depending on the perovskite composition and environmental conditions [73]. Resultingly, the origin of the significant PL emission peak in the Pb inner band is likely based on the combination of experimental evidence and theoretical understanding.

Using TRPL [74,75] study, the carrier lifetime was calculated to be 1.56 ns and 4.02 ns for $CsPbI_3$ at 200 & 250 °C, respectively. In contrast, for $CsSnI_3$, the average lifetime was estimated to be 5.09 ns and 6.24 ns at 200 & 250 °C respectively, as shown in TRPL spectra in Fig. 8 (a & b). Hence, the decay lifetime follows the order (the equation for calculating TRPL was given in the supporting information):

$CsPbI_3$ (250 °C) > $CsPbI_3$ (200 °C) $CsSnI_3$ (250 °C) > $CsSnI_3$ (200 °C)

4.02 > 1.56 6.24 > 5.09.

As among the Pb-based & Pb-free halide perovskites, Pb-free $CsSnI_3$ possess the higher average lifetime at both the synthesis temperatures as compared to $CsPbI_3$ halide perovskites, leading to higher charge separation. Thus, it can be inferred that Pb-free $CsSnI_3$ halide perovskites can be utilised for photovoltaic [76] applications.

The higher average lifetime in $CsSnI_3$, compared with $CsPbI_3$ as determined using TRPL, is generally due to the difference in their respective material properties. It can be explained below based on several experimental parameters, sample quality, and material characteristics as follows.

1. **Band-gap Energy:** $CsSnI_3$ exhibits a slightly larger band-gap than $CsPbI_3$. The larger band gap leads to lower defect density and reduced non-radiative recombination, leading to a longer carrier lifetime.
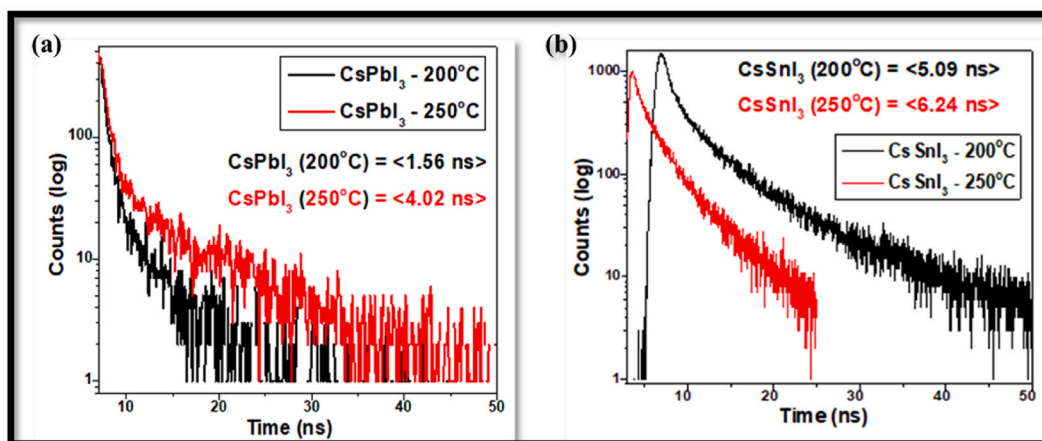

Fig. 8. TRPL spectra of (a) $CsPbI_3$ and (b) $CsSnI_3$ at 200 & 250 °C, respectively.

2. **Crystal Structure:** $CsSnI_3$ exhibits a distorted perovskite structure, while $CsPbI_3$ shows a cubic perovskite structure. These structural differences in Pb & Sn iodide perovskites affect the electronic properties and charge transport within the material, thus affecting the carrier lifetime of $CsSnI_3$ perovskites.

3. **Stability:** $CsSnI_3$ exhibits improved stability in comparison with $CsPbI_3$. The enhanced stability of $CsSnI_3$ results in reduced defect formation and degradation, leading to a higher carrier lifetime for $CsSnI_3$ perovskite.

4. **Lower Ion-Migration:** Ion-migration for Pb ions in $CsPbI_3$ contributes to increased defect formation and degradation. Meanwhile, in $CsSnI_3$ perovskite, the absence of Pb-ions shows lower ion migration, leading to enhanced stability and longer carrier lifetime.

5. **Electronic Structure:** The electronic structure of $CsSnI_3$ and $CsPbI_3$ directly influences the carrier dynamics. $CsSnI_3$ shows a lower density of states near the valence band edge, resulting in reduced trap-assisted recombination compared to $CsPbI_3$. This leads to longer carrier lifetimes in $CsSnI_3$.

6. **Modified Energy Levels:** The energy levels and band structure of $CsSnI_3$ are different from Pb-based halide perovskites. These differences affect the recombination pathways and favour radiative recombination, leading to a longer carrier lifetime of $CsSnI_3$ perovskite.

These differences in the material characteristics of $CsSnI_3$ from Pb-halide perovskites lead to the larger carrier lifetimes in Sn-iodide perovskites.

$CsPbI_3$ and $CsSnI_3$ perovskites are synthesised using the hot-injection method at different temperatures of 200 & 250 °C. As per the literature, the Pb & Sn-based perovskites exhibit the bandgap in the 1.5–1.7 eV range. However, the Cs-based Pb & Sn halide perovskites discussed in this manuscript show a higher bandgap in the range of >3 eV due to experimental limitations (working in an open environment rather than in a glove box and hence, oxidation of Sn is unavoidable). Moreover, the $CsPbI_3$ has oxidized and converted to the yellow phase of $CsPbI_3$, while the Sn^{2+} in $CsSnI_3$ has been oxidized to Sn^{4+} in $CsSnI_3$. However, experiments are repeated 2–3 times, and the original results have been reported in the manuscript with the formation of Pb-based & Pb-free perovskites. Secondly, this discrepancy of PL peak position with UV band-gap arises due to material defects or changes in the electronic structure of the perovskites [77,78]. The XRD pattern shows the undefined peaks for both the perovskites, which are defined as material impurities that signify the defects in the synthesised perovskite material. The defect passivation also leads to the non-agreement of the band gap with the PL peak position [79].

Secondly, the literature reported that $CsPbI_3$-based solar cells have achieved power conversion efficiency (PCE) of over 20 %, while $CsSnI_3$-based solar cells show a PCE of only around 10 %. This is due to the difference in both materials' electronic band structure and stability. CsPbI3 is stable at higher temperatures and has a suitable band gap for photovoltaic applications. On the other hand, $CsSnI_3$ is known to undergo structural phase transitions that affect its stability and performance in solar cells. In the case of $CsSnI_3$, Sn is very unstable and frequently gets oxidized from Sn (II) to Sn (IV) during the fabrication of $CsSnI_3$-based perovskites, leading to low PCE values as compared to Pb-based counterparts. However, in our manuscript, the deviation in bandgap arises due to experimental limitations (working in an open environment rather than in a glove box and hence, oxidation of Sn is unavoidable) that leads to simulation error and yields the variation in the % efficiency in comparison to the reported value. Moreover, research and optimization efforts are being carried out to improve the performance of $CsSnI_3$-based solar cells.
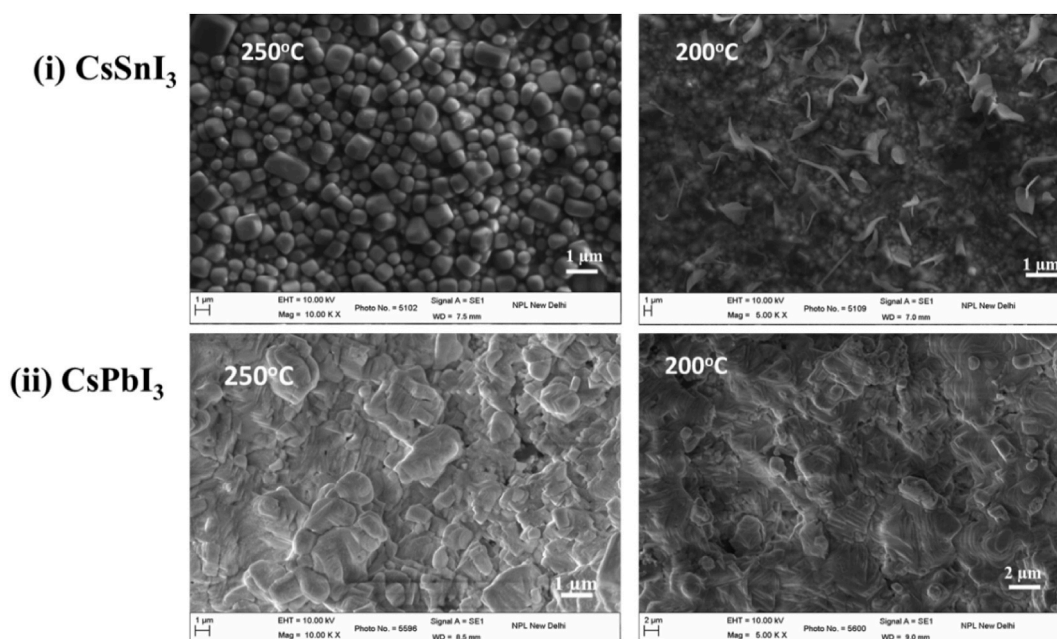

Fig. 9. FE-SEM images for (i) $CsSnI_3$ and (ii) $CsPbI_3$ at 250 °C & 200 °C, respectively.

5.3. FE-SEM study

Fig. 9 demonstrates the surface morphology of the CsSnI$_3$ and CsPbI$_3$ perovskites recorded at different temperatures of 250 °C & 200 °C using FE-SEM operating at 15 keV. The FE-SEM micrographs of CsSnI$_3$ show thin nano-flakes at 200 °C, and cubic nanocrystals of CsSnI$_3$ were observed at 250 °C.

Conversely, the network-type structure was observed at 200 °C, and stacked spherical nanocrystal morphology was observed for CsPbI$_3$ at 250 °C. All the perovskites show minimal accumulation, which may also arise because of the surface charge on the nanocrystals [80]. The corresponding mean diameter observed from each SEM image lies between 50 and 60 nm for CsSnI$_3$, while it lies in the range of 15–22 nm for CsPbI$_3$, which agrees with the TEM data.

5.4. TEM study

The morphology and particle-size distribution of CsSnI$_3$ and CsPbI$_3$ perovskites were recorded using TEM, as shown in Fig. 10. The TEM images of CsPbI$_3$ halide perovskites confirm the presence of spherical particles with their uniform monodisperse distribution. In contrast, Pb-free CsSnI$_3$ perovskite appears as cubic nanocrystals with a polydisperse distribution.

The average size of particles was defined by selecting around 70–80 particles in each image. It was depicted in Fig. 10 that a large size variation was observed in Pb-free halide perovskites in comparison with Pb-based halide perovskites. This implies that particle size varies in Pb-based and Pb-free halide perovskites based on the change in divalent cation in the perovskite lattice structure. In CsPbI$_3$, particle size was calculated to be 12–15 nm, while in CsSnI$_3$, particle size was estimated to be around 75–80 nm[81]. The larger particle size of CsPbI$_3$ led to a lower surface area, favouring higher charge separation.

In comparison, the smaller particle size of CsPbI$_3$ tends to have more inadequate charge separation with a higher surface area. Here, the SAED pattern shows the polycrystalline nature of CsSnI$_3$ and the crystalline nature of CsPbI$_3$ halide perovskites [29,30]. However, it was noticed that the particle size of all halide perovskites lies close to the crystallite size, which was calculated using the W–H plot in XRD data. The TEM histogram represents the particle size distribution (Gaussian distribution) of Pb-based & Pb-free halide perovskites samples.

The limitations in the study of Cs-based lead & lead-free halide perovskites in the literature have been discussed in the recapitulative table (Table 4). On the other hand, this table also discussed how the authors have tried to fill these gaps or limitations in their present work.

6. Thickness effect on output parameters of solar-cell: A simulation study

One of the essential aspects in optimising a solar cell is the absorber layer's thickness, which should be carefully selected to increase the current density. A solar cell's current density and efficiency are reduced by inadequate light absorption. Therefore, having a thin absorber layer is not advantageous. However, a thick absorber layer is not the best choice since it lengthens the path that
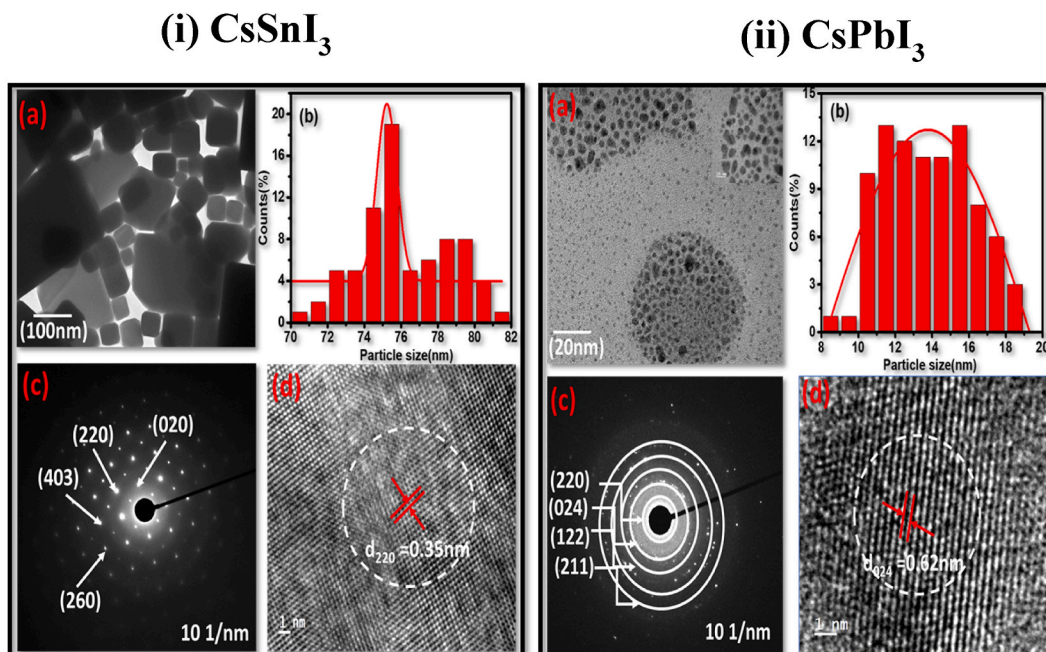

Fig. 10. (a) TEM images, (b) Particle size distribution, (c) SAED patterns, and (d) Lattice spacing for (i) CsSnI$_3$ and (ii) CsPbI$_3$ perovskites.

Table 4

Recapitulative table discussing the gaps treated in present work with respect to reported limitations.

S. No.	Material	Limitations in the related works	Gaps treated in present work	References
1.	$CsPbI_3$ & $CsSnI_3$	Controlling the size of Cs-based Pb & Pb-free perovskite material.	To study different factors for controlling the size of perovskite materials initiated with temperature variation.	[82,83]
2.	$CsPbI_3$ & $CsSnI_3$	The structural stability of hybrid perovskite is poor due to organic cations that hinder commercial applications.	Organic cation is replaced with inorganic cation Cs.	[84]
3.	$CsPbI_3$	The cubic phase is stable at higher temperatures (200–300 °C), while it easily converts to an undesirable non-perovskite δ-phase at room temperature.	Higher temperature (200 & 250 °C) is required to synthesise and optimise temperature to obtain desired phase Pb-based perovskites.	[85]
4.	$CsPbI_3$ & $CsSnI_3$	Inorganic halide perovskite degraded due to instability with respect to moisture and heat.	Studied the simulation properties to tackle the thermal instability properties of perovskites.	[86]
5.	$CsPbI_3$	Volatility of CsPbI3 with time.	The properties need to be improved to enhance the stability and photovoltaic performance of $CsPbI_3$.	[83]

photogenerated charge carriers must travel, which increases the recombination. For a suitable solar cell, selecting the appropriate absorber thickness is crucial.

The n-layer thickness is less than the p-layer thickness, so the photons can pass through the layers without being absorbed or transformed into electron/hole pairs since their breadth will be smaller than the hole's diffusion length. Then, due to their separation in the intrinsic electric field, holes in the n-layer quickly diffuse to the metal electrode before recombination.

In the case of organic solar cells, incomplete conversion of absorber material could lead to non-photoactive phases, which can act as trap states for charge carriers. The FF is lower because the voltage drops due to the series resistance Rs of a solar cell. With the increasing thickness of the layer, the overall electric field strength is decreased, and a quasi-neutral region is formed in the absorber layer. Besides, creating a quasi-neutral layer implies that the carriers transport through diffusion rather than drift, leading to a decrease of FF through increased series resistance. On the other hand, with an increase in thickness from the optimum value, V_{OC} increases, indicating that the recombination in the quasi-neutral region is not dominant.

In addition to improving light absorption, the chance of carrier recombination also increases simultaneously with the increasing thickness of the absorber layer because the charge carriers have to travel longer distances for diffusion in a thicker absorber layer. Therefore, the rise in thickness leads to the nearly saturated fill factor.

In the present work, a perovskite-based solar structure is simulated, as discussed in the introduction. The thickness of the absorber layers ($CsSnI_3$ and $CsPbI_3$) varies from 50 to 250 nm. The results depicted that the output parameters such as open-circuit voltage (V_{OC}), current density (J_{SC}), fill factor (FF), and efficiency vary with the thickness variation, as shown in Figs. 11 and 12. V_{OC}, J_{SC}, and efficiency increased with an increase in thickness. FF was not much affected by thickness variation. After 250 nm thickness, efficiency was significantly less enhanced. Thus, we take 250 nm as the optimized thickness for both layers. At 250 nm, V_{oc}, J_{sc}, FF and efficiency for $CsPbI_3$ are obtained as 0.88 V, 16.87 mA/cm^2, 25.1 % and 3.76 %, respectively, and for $CsSnI_3$-based structure, V_{OC}, J_{SC}, FF and efficiency are achieved as 0.89 V, 27.2 mA/cm^2, 25.11 % and 6.11 %, respectively. The overall performance in terms of efficiency and FF at optimized conditions for both layers-based structures is shown as a bar graph (Fig. 13).

Generally, the efficiency of a solar cell depends on various factors, including material properties, film quality, device architecture, and optimization of device parameters. Here, the simulation results conclude that $CsSnI_3$ is a better absorber material than $CsPbI_3$ in terms of efficiency with respect to thickness variation due to the following reasons.

1. **Bandgap and Light Absorption:** The bandgap for $CsSnI_3$ aligns well with the solar spectrum and is more suitable for absorbing solar radiation than $CsPbI_3$. Thus, $CsSnI_3$ absorbs the more significant portion of sunlight and converts it into electrical energy. However, the optimized thickness ensures that $CsSnI_3$ maximizes light absorption within its ideal bandgap range, leading to higher efficiency.

2. **Optical Properties:** $CsSnI_3$ shows superior optical properties compared to $CsPbI_3$, such as a higher absorption coefficient or a broader absorption range. These properties enhance light harvesting and solar cell efficiency. The $CsSnI_3$ film can be tuned by optimising the thickness to maximize the light absorption, resulting in improved efficiency.

3. **Charge Carrier Dynamics:** $CsSnI_3$ exhibits more favourable charge carrier dynamics than $CsPbI_3$. This could include higher carrier mobility, longer carrier lifetimes, or reduced non-radiative recombination rates. Optimising the thickness helps achieve the ideal charge carrier dynamics for $CsSnI_3$, leading to better charge extraction and reduced losses, resulting in higher efficiency.

4. **Film Quality and Defects:** Optimized thickness may also help achieve improved film quality for CsSnI3. A more uniform and defect-free film enhances the charge transport and reduces non-radiative recombination, leading to higher efficiency. $CsSnI_3$ films with optimized thickness may have a reduced density of defects or improved surface passivation, contributing to improved device performance.

5. **Thickness-Dependent Absorption and Carrier Collection:** The absorption of light and collection of charge carriers can be influenced by the thickness of the perovskite film. Optimising the thickness of the $CsSnI_3$ film can ensure an optimal balance between light absorption and charge extraction. The optimized thickness may enhance photon absorption while minimizing carrier recombination, resulting in higher efficiency.
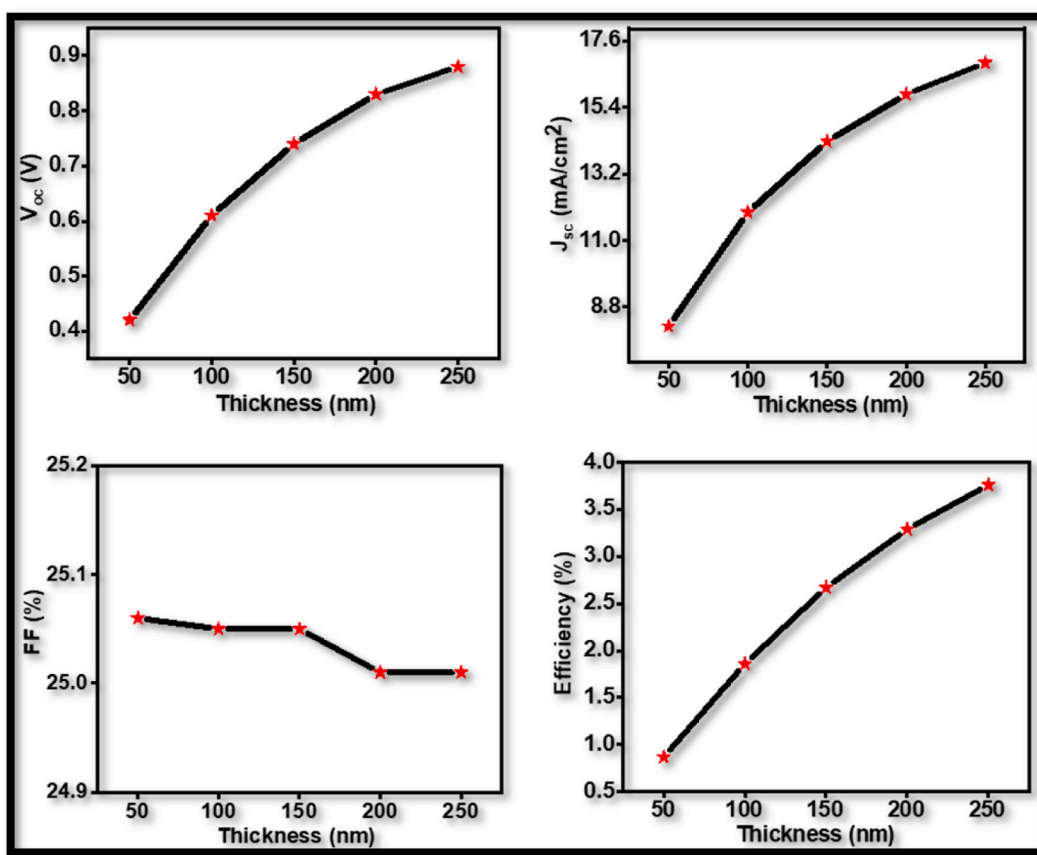
Fig. 11. Effect of CsPbI$_3$ thickness on V$_{OC}$, J$_{SC}$, FF and device efficiency.

7. Conclusion

In conclusion, we have synthesised the Pb-based & Pb-free CsPbI$_3$ and CsSnI$_3$ halide perovskites using the Hot-injection method at 200 & 250 °C. Here, XRD confirmed the perovskite crystal structure and tuned the optical band gap for the Pb-based & Pb-free halide perovskites based on temperature variation. The PL & TRPL study shows the variation in the photoluminescence efficiency of Pb-based and Pb-free halides. We have studied the variation in experimental and theoretical parameters in Pb-based & Pb-free halide perovskites based on variation in temperature. It was also determined that hot-injection synthesised Sn-based halide perovskites remained stable for a prominent period. Sn (II) will not oxidise into Sn (IV) during the synthesis because synthesis will be performed under an argon atmosphere. However, the TRPL study also signifies that CsSnI$_3$ perovskite exhibits a higher average lifetime than Pb-based halide perovskites. Thus, Sn can be an alternative for Pb-free perovskite-based optoelectronic devices. Both the perovskites (CsPbI$_3$ and CsSnI$_3$) based solar structures have been compared by optimising their thickness with the help of simulation, and results stated that CsSnI$_3$ (6.11 %) is a better absorber material as compared to CsPbI$_3$ (3.76 %) in terms of efficiency. However, all the parameters in the simulation study have shown improved characteristics for CsSnI$_3$ perovskites compared to Pb-based halide perovskites. This signifies that CsSnI3 perovskites show enhanced properties when Pb-based and Pb-free halide perovskites are synthesised using the hot-injection method. Therefore, Sn-based halide perovskites are known to be potential candidates for optoelectronic applications. This experimental and theoretical comparative study of the hot-injection method synthesised CsPbI$_3$ and CsSnI$_3$ perovskites are rarely investigated for optoelectronic applications.

Impact statement

Metal halide Pb-based and Pb-free perovskite crystal structures are an essential class of optoelectronic materials due to their significant optoelectronic properties, optical absorption, and tuneable emission spectrum properties. Replacing the toxic Pb with Pb-free alternatives (such as tin (Sn)) for diverse photovoltaic and optoelectronic applications is essential. Moreover, replacing the volatile methylammonium (MA) with cesium (Cs) leads to an efficient perovskite absorber layer with improved optical and thermal stability and stabilized photoconversion efficiency.

This paper discusses the correlation between the experimental and theoretical work for the Pb-based and Pb-free perovskites
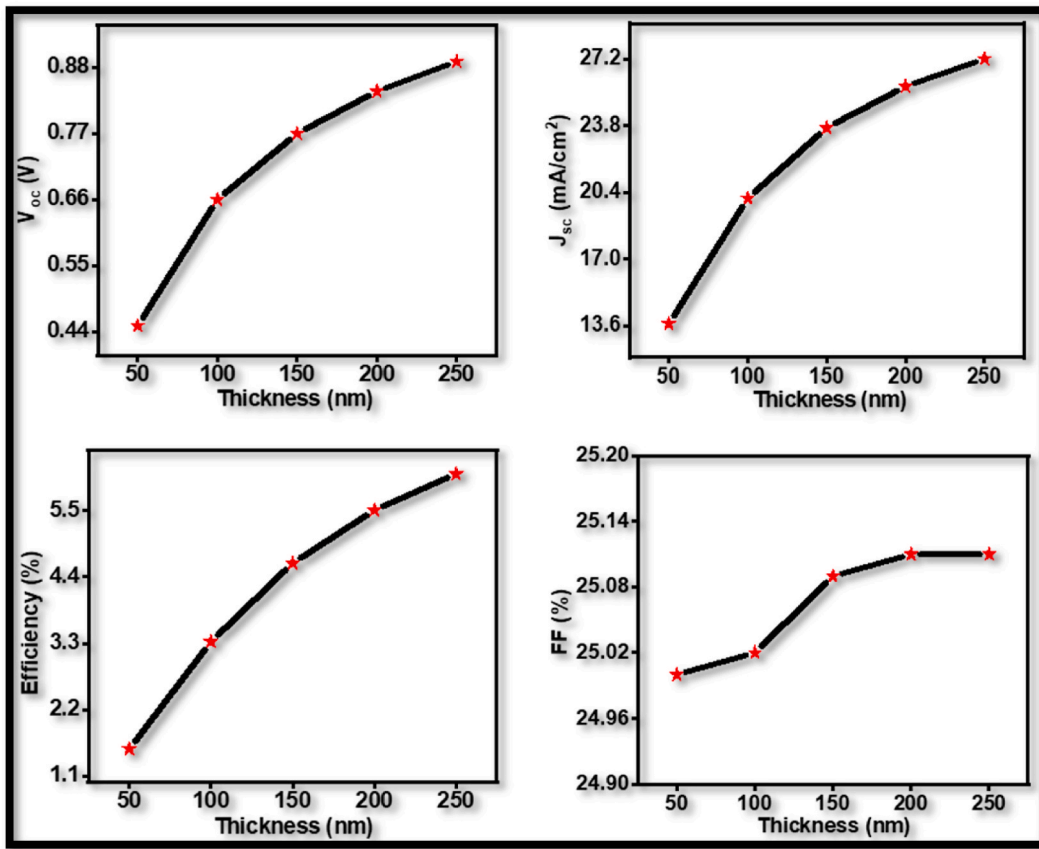
Fig. 12. Effect of $CsSnI_3$ thickness on V_{oc}, J_{sc}, FF and efficiency of the device.
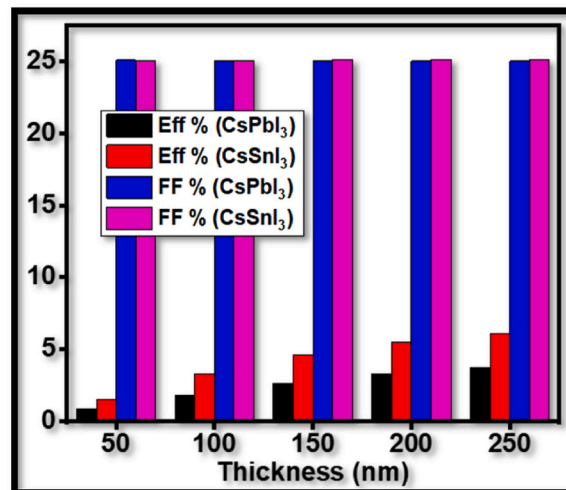

Fig. 13. Overall performance of $CsPbI_3$ and $CsSnI_3$-based solar structure at various thicknesses.

synthesised using the hot-injection method at different temperatures. Here, the structural, optical, and morphological properties of Pb-based and Pb-free halide perovskites were studied using XRD, UV–Vis, PL, FE-SEM, and TEM characterisations with temperature variation. The studies reveal that in contrast with $CsPbI_3$, Sn-based halides exhibit a higher band-gap (3.73 eV) with a decrease in size and higher average lifetime (5.09 ns) at a lower temperature, indicating an efficient replacement of Pb with Sn for Pb-free halides.

Simulation is also carried out using the help of SCAPS-1D software to study the effect of various parameters of $CsSnI_3$ and $CsPbI_3$

layers on solar cell performance. Results stated that the CsSnI$_3$ (6.11 %) based solar structure depicts higher efficiency than CsPbI$_3$ (3.76 %). This approach can give an insight into how the thickness of layers impacts the output characteristics of the device.

The experimental and theoretical comparative study of the hot-injection method synthesised CsPbI3 and CsSnI3 perovskites are rarely investigated for optoelectronic applications.

CRediT authorship contribution statement

Sonali Mehra: Writing – original draft, Investigation, Formal analysis, Data curation, Conceptualization. **Mamta:** Investigation, Data curation, Investigation, Data curation. **Jai Tawale:** Investigation. **Govind Gupta:** Investigation. **V.N. Singh:** Writing – review & editing, Investigation. **A.K. Srivastava:** Supervision. **Shailesh Narain Sharma:** Writing – review & editing, Supervision.

Declaration of competing interest

The authors declare that they have no competing financial interests or personal relationships that could have appeared to influence the work reported in this manuscript.

Acknowledgement

References

[1] C.C. Li, T. Yu Huang, Y.H. Lai, Y.C. Huang, C. Shan Tan, Materials Today Electronics 8 (2024) 100095.
[2] H. Dong, C. Ran, W. Gao, M. Li, Y. Xia, W. Huang, eLight 3 (2023) 3.
[3] A. Wang, C. Zuo, X. Niu, L. Ding, J. Ding, F. Hao, Chem. Eng. J. 451 (2023) 138926.
[4] H. Bencherif, Sol. Energy 238 (2022) 114–125.
[5] D. Drozdowski, A. Gągor, D. Stefańska, J.K. Zaręba, K. Fedoruk, M. Mączka, A. Sieradzki, J. Phys. Chem. C 126 (2022) 1600–1610.
[6] M. Maczka, A. Gagor, J.K. Zaręba, D. Stefanska, M. Drozd, S. Balciunas, M. Šimėnas, J. Banys, A. Sieradzki, Chem. Mater. 32 (2020) 4072–4082.
[7] O.I. Kucheriv, V.Y. Sirenko, H.R. Petrosova, V.A. Pavlenko, S. Shova, I.A. Gural'skiy, Inorg. Chem. Front. 10 (2023) 1039. D3QI00872J.
[8] V. Raptis, A. Kaltzoglou, J. Phys. Chem. Solid. 180 (2023) 111383.
[9] I. López-Fernández, D. Valli, C. Wang, S. Samanta, T. Okamoto, Y. Huang, K. Sun, Y. Liu, V.S. Chirvony, A. Patra, J. Zito, L. De Trizio, D. Gaur, H. Sun, Z. Xia, X. Li, H. Zeng, I. Mora-Seró, N. Pradhan, J.P. Martínez-Pastor, P. Müller-Buschbaum, V. Biju, T. Debnath, M. Saliba, E. Debroye, R.L.Z. Hoye, I. Infante, L. Manna, L. Polavarapu, Adv Funct Materials 34 (2024) 2307896.
[10] S. Mehra, J. Saroha, E. Rani, V. Sharma, L. Goswami, G. Gupta, A.K. Srivastava, S.N. Sharma, Opt. Mater. 136 (2023) 113344.
[11] S. Mehra, S. Bishnoi, A. Jaiswal, M. Jagadeeswararao, A.K. Srivastava, S.N. Sharma, P. Vashishtha, Energy Storage 2 (2020) e120.
[12] D.-Y. Kim, J.-G. Jung, Y.-J. Lee, M.-H. Park, Materials 16 (2023) 6317.
[13] Z.-K. Tan, R.S. Moghaddam, M.L. Lai, P. Docampo, R. Higler, F. Deschler, M. Price, A. Sadhanala, L.M. Pazos, D. Credgington, F. Hanusch, T. Bein, H.J. Snaith, R. H. Friend, Nature Nanotech 9 (2014) 687–692.
[14] S. Yakunin, L. Protesescu, F. Krieg, M.I. Bodnarchuk, G. Nedelcu, M. Humer, G. De Luca, M. Fiebig, W. Heiss, M.V. Kovalenko, Nat. Commun. 6 (2015) 8056.
[15] B.-W. Park, B. Philippe, X. Zhang, H. Rensmo, G. Boschloo, E.M.J. Johansson, Adv. Mater. 27 (2015) 6806–6813.
[16] M.H. Kumar, S. Dharani, W.L. Leong, P.P. Boix, R.R. Prabhakar, T. Baikie, C. Shi, H. Ding, R. Ramesh, M. Asta, M. Graetzel, S.G. Mhaisalkar, N. Mathews, Adv. Mater. 26 (2014) 7122–7127.
[17] N.K. Noel, S.D. Stranks, A. Abate, C. Wehrenfennig, S. Guarnera, A.-A. Haghighirad, A. Sadhanala, G.E. Eperon, S.K. Pathak, M.B. Johnston, A. Petrozza, L. M. Herz, H.J. Snaith, Energy Environ. Sci. 7 (2014) 3061–3068.
[18] S. Mehra, A.K. Chauhan, S. Dodeja, P. Kumar, L. Goswami, G. Gupta, A.K. Srivastava, S.N. Sharma, Opt. Mater. 142 (2023) 114014.
[19] S. Mehra, R. Pandey, J. Madan, R. Sharma, L. Goswami, G. Gupta, V.N. Singh, A.K. Srivastava, S.N. Sharma, ChemistryOpen 13 (2024) e202300055.
[20] G. Nedelcu, L. Protesescu, S. Yakunin, M.I. Bodnarchuk, M.J. Grotevent, M.V. Kovalenko, Nano Lett. 15 (2015) 5635–5640.
[21] D. Di, K.P. Musselman, G. Li, A. Sadhanala, Y. Ievskaya, Q. Song, Z.-K. Tan, M.L. Lai, J.L. MacManus-Driscoll, N.C. Greenham, R.H. Friend, J. Phys. Chem. Lett. 6 (2015) 446–450.
[22] H. Bencherif, L. Dehimi, N. Mahsar, E. Kouriche, F. Pezzimenti, Mater. Sci. Eng., B 276 (2022) 115574.
[23] M.L. Böhm, T.C. Jellicoe, J.P.H. Rivett, A. Sadhanala, N.J.L.K. Davis, F.S.F. Morgenstern, K.C. Gödel, J. Govindasamy, C.G.M. Benson, N.C. Greenham, B. Ehrler, J. Phys. Chem. Lett. 6 (2015) 3510–3514.
[24] M. Mammeri, L. Dehimi, H. Bencherif, F. Pezzimenti, Sol. Energy 249 (2023) 651–660.
[25] L. Protesescu, S. Yakunin, M.I. Bodnarchuk, F. Krieg, R. Caputo, C.H. Hendon, R.X. Yang, A. Walsh, M.V. Kovalenko, Nano Lett. 15 (2015) 3692–3696.
[26] S. Mehra, U. Kumar, A. Mehta, A.K. Srivastava, S. Chand, S.N. Sharma, J. Nanosci. Nanotechnol. 20 (2020) 3809–3815.
[27] Z. Xiao, Y. Zhou, H. Hosono, T. Kamiya, Phys. Chem. Chem. Phys. 17 (2015) 18900–18903.
[28] T. Pons, I.L. Medintz, D. Farrell, X. Wang, A.F. Grimes, D.S. English, L. Berti, H. Mattoussi, Small 7 (2011) 2101–2108.
[29] Q. Chen, N. De Marco, Y. Michael Yang, T.-B. Song, C.-C. Chen, H. Zhao, Z. Hong, H. Zhou, Y. Yang, Nano Today 10 (2015) 355–396.
[30] X. Li, W. Ma, D. Liang, W. Cai, S. Zhao, Z. Zang, eScience 2 (2022) 646–654.
[31] Q. Zhuang, C. Zhang, C. Gong, H. Li, H. Li, Z. Zhang, H. Yang, J. Chen, Z. Zang, Nano Energy 102 (2022) 107747.
[32] J. Ye, M.M. Byranvand, C.O. Martínez, R.L.Z. Hoye, M. Saliba, L. Polavarapu, Angew. Chem. 133 (2021) 21804–21828.
[33] S. MehraMamta, V.N. Singh, G. Gupta, A.K. Srivastava, S.N. Sharma, Heliyon 9 (2023) e21701.
[34] H. Bencherif, L. Dehimi, F. Pezzimenti, A. Yousfi, in: 2018 International Conference on Applied Smart Systems (ICASS), IEEE, Medea, Algeria, 2018, pp. 1–6.
[35] H. Bencherif, L. Dehimi, F. Pezzimenti, A. Yousfi, M.A. Abdi, L. Saidi, F.G.D. Corte, Optik 223 (2020) 165346.
[36] T.C. Jellicoe, J.M. Richter, H.F.J. Glass, M. Tabachnyk, R. Brady, S.E. Dutton, A. Rao, R.H. Friend, D. Credgington, N.C. Greenham, M.L. Böhm, J. Am. Chem. Soc. 138 (2016) 2941–2944.
[37] A. Naskar, R. Khanal, S. Choudhury, Materials 14 (2021) 1032.
[38] Q.A. Akkerman, V. D'Innocenzo, S. Accornero, A. Scarpellini, A. Petrozza, M. Prato, L. Manna, J. Am. Chem. Soc. 137 (2015) 10276–10281.
[39] F. Meddour, H. Bencherif, A. Boukarkar, M.A. Abdi, M. Amir, Optik 208 (2020) 164022.
[40] M. Burgelman, J. Verschraegen, S. Degrave, P. Nollet, Prog. Photovolt: Res. Appl. 12 (2004) 143–153.

[41] A. Swarnkar, A.R. Marshall, E.M. Sanehira, B.D. Chernomordik, D.T. Moore, J.A. Christians, T. Chakrabarti, J.M. Luther, Science 354 (2016) 92–95.
[42] C.K. Ng, W. Yin, H. Li, J.J. Jasieniak, Nanoscale 12 (2020) 4859–4867.
[43] L.A. Frolova, D.V. Anokhin, A.A. Piryazev, S. Yu Luchkin, N.N. Dremova, K.J. Stevenson, P.A. Troshin, J. Phys. Chem. Lett. 8 (2017) 67–72.
[44] E.M. Hutter, T.J. Savenije, ACS Energy Lett. 3 (2018) 2068–2069.
[45] F. Li, S. Zhou, J. Yuan, C. Qin, Y. Yang, J. Shi, X. Ling, Y. Li, W. Ma, ACS Energy Lett. 4 (2019) 2571–2578.
[46] H. Choi, J. Jeong, H.-B. Kim, S. Kim, B. Walker, G.-H. Kim, J.Y. Kim, Nano Energy 7 (2014) 80–85.
[47] T.S. Ripolles, K. Nishinaka, Y. Ogomi, Y. Miyata, S. Hayase, Sol. Energy Mater. Sol. Cell. 144 (2016) 532–536.
[48] X. Ling, S. Zhou, J. Yuan, J. Shi, Y. Qian, B.W. Larson, Q. Zhao, C. Qin, F. Li, G. Shi, C. Stewart, J. Hu, X. Zhang, J.M. Luther, S. Duhm, W. Ma, Adv. Energy Mater. 9 (2019) 1900721.
[49] L.-J. Chen, C.-R. Lee, Y.-J. Chuang, Z.-H. Wu, C. Chen, J. Phys. Chem. Lett. 7 (2016) 5028–5035.
[50] K.P. Marshall, R.I. Walton, R.A. Hatton, J. Mater. Chem. A 3 (2015) 11631–11640.
[51] X. Qiu, B. Cao, S. Yuan, X. Chen, Z. Qiu, Y. Jiang, Q. Ye, H. Wang, H. Zeng, J. Liu, M.G. Kanatzidis, Sol. Energy Mater. Sol. Cell. 159 (2017) 227–234.
[52] K. K. Maurya Mamta, V.N. Singh, Coatings 12 (2022) 405.
[53] S. Srivast, A.K. Singh, P. Kumar, B. Pradhan, Comparative performance analysis of lead-free perovskites solar cells by numerical simulation, in: Review, 2021.
[54] D. Jayan K, V. Sebastian, J. Kurian, Sol. Energy 221 (2021) 99–108.
[55] A.B. Coulibaly, S.O. Oyedele, N.R. Kre, B. Aka, MNSMS (2019) 97–107, 09.
[56] Z. Kang, X. Yan, Y. Wang, Z. Bai, Y. Liu, Z. Zhang, P. Lin, X. Zhang, H. Yuan, X. Zhang, Y. Zhang, Sci. Rep. 5 (2015) 7882.
[57] G.K. Williamson, W.H. Hall, Acta Metall. 1 (1953) 22–31.
[58] P. Kumar, S. Pathak, A. Singh, K. Jain, H. Khanduri, L. Wang, S.-K. Kim, R.P. Pant, J. Mater. Chem. C 10 (2022) 12652–12679.
[59] N. Adeela, K. Maaz, U. Khan, S. Karim, A. Nisar, M. Ahmad, G. Ali, X.F. Han, J.L. Duan, J. Liu, J. Alloys Compd. 639 (2015) 533–540.
[60] S. Talukdar, D. Mandal, K. Mandal, Chem. Phys. Lett. 672 (2017) 57–62.
[61] M.D. Smith, B.A. Connor, H.I. Karunadasa, Chem. Rev. 119 (2019) 3104–3139.
[62] P. Kumar, S. Pathak, A. Singh, Kuldeep, H. Khanduri, X. Wang, G.A. Basheed, R.P. Pant, Mater. Chem. Phys. 265 (2021) 124476.
[63] A. Manikandan, L.J. Kennedy, M. Bououdina, J.J. Vijaya, J. Magn. Magn Mater. 349 (2014) 249–258.
[64] H.-S. Kim, C.-R. Lee, J.-H. Im, K.-B. Lee, T. Moehl, A. Marchioro, S.-J. Moon, R. Humphry-Baker, J.-H. Yum, J.E. Moser, M. Grätzel, N.-G. Park, Sci. Rep. 2 (2012) 591.
[65] M.M. Rashad, A.M. Hassan, A.M. Nassar, N.M. Ibrahim, A. Mourtada, Appl. Phys. A 117 (2014) 877–890.
[66] C. Bi, Y. Yuan, Y. Fang, J. Huang, Adv. Energy Mater. 5 (2015) 1401616.
[67] B. Conings, J. Drijkoningen, N. Gauquelin, A. Babayigit, J. D'Haen, L. D'Olieslaeger, A. Ethirajan, J. Verbeeck, J. Manca, E. Mosconi, F.D. Angelis, H.-G. Boyen, Adv. Energy Mater. 5 (2015) 1500477.
[68] E. Edri, S. Kirmayer, M. Kulbak, G. Hodes, D. Cahen, J. Phys. Chem. Lett. 5 (2014) 429–433.
[69] X. Wang, W. Meng, W. Liao, J. Wang, R.-G. Xiong, Y. Yan, J. Phys. Chem. Lett. 10 (2019) 501–506.
[70] L. Mao, Y. Wu, C.C. Stoumpos, M.R. Wasielewski, M.G. Kanatzidis, J. Am. Chem. Soc. 139 (2017) 5210–5215.
[71] J.-Y. Jiang, Q. Xu, J.-J. Ma, Z.-X. Gong, C. Shi, Y. Zhang, Dalton Trans. 49 (2020) 16860–16865.
[72] G. Teri, Q.-Q. Jia, Q. Guo, Y. Zhang, D.-W. Fu, Sci. China Mater. 66 (2023) 3687–3695.
[73] H. Zhu, G. Liu, B. Sun, Y. Dong, S. Zhang, B. Xu, Y. Zou, H. Zeng, Sol. RRL 7 (2023) 2300754.
[74] P. Kumar, S. Pathak, K. Jain, A. Singh, Kuldeep, G.A. Basheed, R.P. Pant, J. Alloys Compd. 904 (2022) 163992.
[75] N. Jain, N. Marwaha, R. Verma, B.K. Gupta, A.K. Srivastava, RSC Adv. 6 (2016) 4960–4968.
[76] M.A. Afroz, A. Singh, R.K. Gupta, R. Garai, N.K. TailorYukta, S. Choudhary, B. Sharma, P. Mahajan, B. Padha, S. Verma, S. Arya, V. Gupta, S. Akin, D. Prochowicz, M.M. Tavakoli, S.P. Singh, P.K. Iyer, P. Yadav, H. Hu, G. De, S. Satapathi, J. Mater. Chem. A 11 (2023) 13133–13173.
[77] H.F. Liang, C.T.G. Smith, C.A. Mills, S.R.P. Silva, J. Mater. Chem. C 3 (2015) 12484–12491.
[78] A. Chaves, J.G. Azadani, H. Alsalman, D.R. Da Costa, R. Frisenda, A.J. Chaves, S.H. Song, Y.D. Kim, D. He, J. Zhou, A. Castellanos-Gomez, F.M. Peeters, Z. Liu, C. L. Hinkle, S.-H. Oh, P.D. Ye, S.J. Koester, Y.H. Lee, Ph Avouris, X. Wang, T. Low, npj 2D Mater Appl 4 (2020) 29.
[79] S. Mehra, A.K. Chauhan, S. Dodeja, P. Kumar, L. Goswami, G. Gupta, A.K. Srivastava, S.N. Sharma, Opt. Mater. 142 (2023) 114014.
[80] C.C. Stoumpos, C.D. Malliakas, M.G. Kanatzidis, Inorg. Chem. 52 (2013) 9019–9038.
[81] D.B. Williams, C.B. Carter, in: Transmission Electron Microscopy, Springer US, Boston, MA, 2009, pp. 53–71.
[82] L. Lin, L. Jiang, P. Li, H. Xiong, Z. Kang, B. Fan, Y. Qiu, Sol. Energy 198 (2020) 454–460.
[83] A. Gamal, M. Alruqi, M. Rabia, Intl J of Energy Research 46 (2022) 21739–21756.
[84] D. Liu, W. Zha, Y. Guo, R. Sa, ACS Omega 5 (2020) 893–896.
[85] X. Tan, S. Wang, Q. Zhang, H. Liu, W. Li, L. Zhu, H. Chen, Matter 6 (2023) 691–727.
[86] I.M. Maafa, Nanomaterials 12 (2022) 1651.